

Engineering reconfigurable flow patterns via surface-driven light-controlled active matter

Xingting Gong,¹ Arnold J. T. M. Mathijssen ,^{2,3} Zev Bryant,² and Manu Prakash^{2,*}

¹*Department of Applied Physics, Stanford University, 348 Via Pueblo, Stanford, California 94305, USA*

²*Department of Bioengineering, Stanford University, 443 Via Ortega, Stanford, California 94305, USA*

³*Department of Physics and Astronomy, University of Pennsylvania, 209 South 33rd Street, Philadelphia, Pennsylvania 19104, USA*



(Received 3 November 2020; accepted 19 November 2021; published 30 December 2021)

Surface-driven flows are ubiquitous in nature, from subcellular cytoplasmic streaming to organ-scale ciliary arrays. Here we model how confined geometries can be used to engineer complex hydrodynamic patterns driven by activity prescribed solely on the boundary. Specifically, we simulate light-controlled surface-driven active matter, probing the emergent properties of a suspension of active colloids that can bind and unbind from surfaces of a closed microchamber, together creating an active carpet. The attached colloids generate large-scale flows that in turn can advect detached particles toward the walls. Switching the particle velocities with light, we program the active suspension and demonstrate a rich design space of flow patterns characterized by topological defects. We derive the possible mode structures and use this theory to optimize different microfluidic functions including hydrodynamic compartmentalization and chaotic mixing. Our results pave the way toward designing and controlling surface-driven active fluids.

DOI: [10.1103/PhysRevFluids.6.123104](https://doi.org/10.1103/PhysRevFluids.6.123104)

I. INTRODUCTION

The ability of biological organisms to self-assemble and organize has inspired new ideas in engineering and physics. Unlike traditional materials, active matter consumes energy at the scale of each individual particle, and local interactions between such particles give rise to complex collective behaviors [1–12]. As such, the self-organizing capability of active matter makes it a fertile ground for new design principles and technologies. However, the realization of such devices is contingent upon our currently limited ability to control or program them [13–17].

As a strategy for designing tunable active matter, we are inspired by the prevalence of surface-driven activity in nature. Rather than programming activity in the bulk, one could potentially prescribe what is on the boundary, which in turn modulates and controls bulk flows. For example, in human airways the coordinated motion of micron-scale cilia across the entire organ drives coherent flows and is essential for mucus clearance [18–20]. Furthermore, cytoplasmic streaming in characean algae is a salient example of surface-driven activity at the subcellular scale: Organelle-carrying myosin motors walk along fixed actin tracks, resulting in macroscopic circulation of the cytoplasm [15,21–24]. Synthetic examples of active surfaces include artificial cilia [25–30], phoretic pumps [31–35], self-propelled droplets and colloids accumulated on walls [36–40], Quincke rollers [36], engineered bacterial carpets [41–43], flows generated by gradients of interfacial tension [44], and molecular motility assays [45].

*manup@stanford.edu

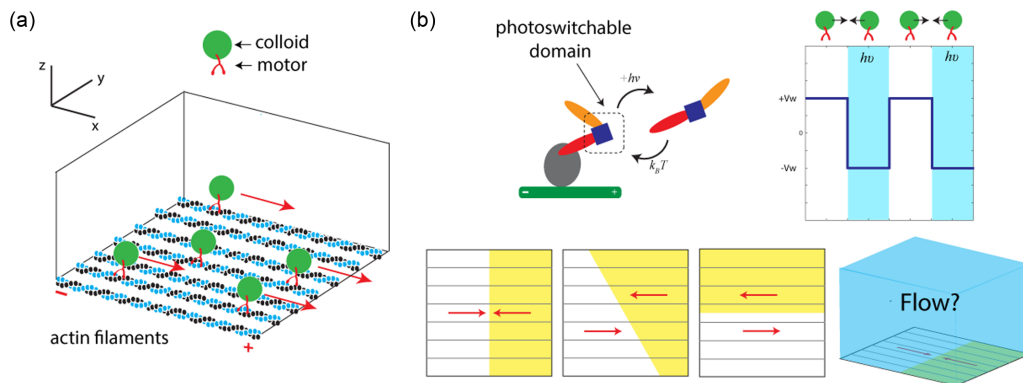


FIG. 1. Experimental proposal for surface-driven flows in confined volumes. (a) *In vitro* reconstitution of cytoplasmic streaming as a basis for engineering flows. Load-carrying molecular motors walk along polarized and aligned actin filaments pinned to a surface. The viscous drag on the load (colloidal particles) imparts momentum in the surrounding fluid, and the action of many such particles can lead to emergent bulk flows. (b) The top shows that molecular motors have been genetically engineered to switch their direction of motion along a filament in response to blue light (see [49]). It is shown on the bottom that, by patterning the boundary with light, one can dynamically control the flow structure of a chamber with spatiotemporal precision.

The ability to micromanipulate flow structures is of great interest for applications such as microfluidics and laboratory-on-a-chip devices [46,47]. Yet miniaturizing self-contained microfluidic devices that do not require external macroscopic pumps and valves has remained a major challenge in the field. A solution could be to instead generate flows internally by injecting momentum from patterned active surfaces [42], but little is understood how such topological patterns affect the flow properties and structures that can emerge across the scales. In other words, while external pressure-driven microfluidics are now ubiquitous in research and industrial applications, the design space of internally driven flows using surface activity in confined geometries is almost entirely unknown. As such, there are two issues to be addressed: the experimental parameters necessary for the realization of surface-driven flows and the elucidation of the design space of active surface patterning.

In the first half of the paper we propose an experimental realization of surface-driven active flows using light-controllable molecular motors (Fig. 1). Light has proven to be a powerful experimental handle in living systems due to its ability to target molecules with high spatiotemporal resolution [16]. Of particular interest to us, engineered cytoskeletal motors incorporating a photosensitive LOV2 domain have been shown to modulate their speed or direction in response to blue light [48,49] [Fig. 1(b)]. We develop an *in silico* model consisting of aligned filament tracks patterned across a single active boundary of a closed rectangular flow chamber [Fig. 1(a)]. Viscous drag on cargo-carrying molecular motors, whose direction along the tracks is switchable by light, impart momentum into their surroundings, entraining the local fluid. We demonstrate that our proposed system is capable of generating macroscopic steady-state flows within a regime of realistic motor properties. We then perturb the system with light to explore the design space of possible flow structures using two fundamental modes we term the head-on and shear defects. In contrast with other theoretical works involving cytoplasmic streaming [23,24], we explicitly consider stochastic dynamics of particles that can attach and detach from the active carpet.

In the second half of the paper we introduce an analytical framework based on the interior squirmer model to further generalize these flow structures and explore the full design space of surface activity. We demonstrate that surface-driven flows can achieve remarkably complex three-dimensional (3D) flow structures with properties like chaotic mixing and particle confinement with no physical barriers. Overall, our results provide insight into boundary-driven flows in naturally

occurring biological systems and pave the way for using surface activity to program reconfigurable bulk flows at small scales.

II. SYSTEM DESCRIPTION

Our *in silico* experiment of surface-driven flows focuses on a closed rectangular chamber, where surfaces can be patterned by actin tracks that are parallel and polarized in orientation [Fig. 2(a)]. Active particles in our system consist of colloids coated with molecular motors [Fig. 2(a), green particles]. These particles are suspended in bulk and can attach to the surface, after which they walk ballistically from the minus to the plus end of the tracks in the absence of light and reverse direction in the presence of light. As these particles move along the surface, they entrain the local fluid and may generate long-range circulating flows. Particles in the bulk are advected by these flows, which in turn can transport them toward the surface, to which they can bind and unbind through probabilities of attachment or detachment.

In previous experiments, aligned tracks have been realized in various settings for over two decades. For example, F-actin can be aligned with electric fields [50]. The polar alignment of microtubules on glass surfaces has also been achieved using hydrodynamic flows [51] or aligned polymerization [52]. Furthermore, the field of engineering molecular motors is becoming more established. Different types of motors have been engineered to walk backward [53], to respond dynamically to calcium signals [54] or to light [48]. Most recently, Ruijgrok *et al.* have demonstrated the directional switching of processive myosin motors in response to blue light [49]. Engineered molecular motors have already found various applications in other synthetic systems, such as the optogenetic control of cytoskeletal suspensions [16,55,56].

Our methods are described in detail in the Supplemental Material [57] (see also Refs. [54,58–68]). In brief, to solve for the system dynamics, we alternate between (i) computing the flow field $\mathbf{u}(\mathbf{r})$ at position \mathbf{r} using a computational fluid dynamics (CFD) solver [58], (ii) integrating the bulk particle motion with Brownian dynamics, and (iii) updating the surface particle density and dynamics. For the first step, inspired by Lighthill [59] and Blake [60], we implement a slip velocity on the active surface due to the motion of the bound particles [Fig. 2(b)]. In the dense particle limit, the surrounding flow will saturate to the particle speed, but in the sparse limit the velocity vanishes. In between, we ignore interparticle interactions and assume that the flow magnitude is approximately linear with respect to particle concentration (see Fig. S1 in [57]). We have additionally validated our CFD solver against a few simple benchmarks (Figs. S2–S5 in [57]).

Detached particles in the bulk are subject to advection and diffusion. Their relative strengths are set by the Péclet number $Pe = LV/D$, where V is the characteristic velocity of the motors, L is the longest chamber length, and D is the diffusion constant. We solve for particle trajectories in the bulk by integrating the Langevin equation in the overdamped limit

$$r_i(t + dt) = u_i(t)dt + \sqrt{2Ddt}\eta_i(t), \quad (1)$$

where i refers to components of the position $\mathbf{r} = \{x, y, z\}$ in Cartesian coordinates, the time step is dt , and $\boldsymbol{\eta}(t)$ is uncorrelated Gaussian white noise defined by $\langle \eta_i(t) \rangle = 0$ and $\langle \eta_i(t)\eta_j(t') \rangle = \delta_{ij}\delta(t - t')$ in terms of the Kronecker and Dirac delta functions.

Particles that approach the surface closer than a cutoff ϵ can attach with rate P_{on} , modeled as a linearly decreasing function of particle density [Fig. 2(c)]. We assume that the particles are otherwise noninteracting. On the boundary, particles walk ballistically with a direction specified by the orientation of the tracks and the pattern of light. Conversely, bound particles can detach from the surface with a constant rate P_{off} [Fig. 2(d)]. Initially, the boundary is uniformly populated with a density equal to half the surface coverage, and no motile particles are initialized in the bulk.

In our model, the important parameters to vary are Pe and P_{off} . The former sets the diffusivity of the active colloids while keeping the chamber geometry and particle velocity constant and the latter has a nice interpretation in terms of motor processivity (average run length before detachment). The other parameters P_{on} and the Reynolds number $Re = \rho VL/\mu$ (with ρ and μ the density and

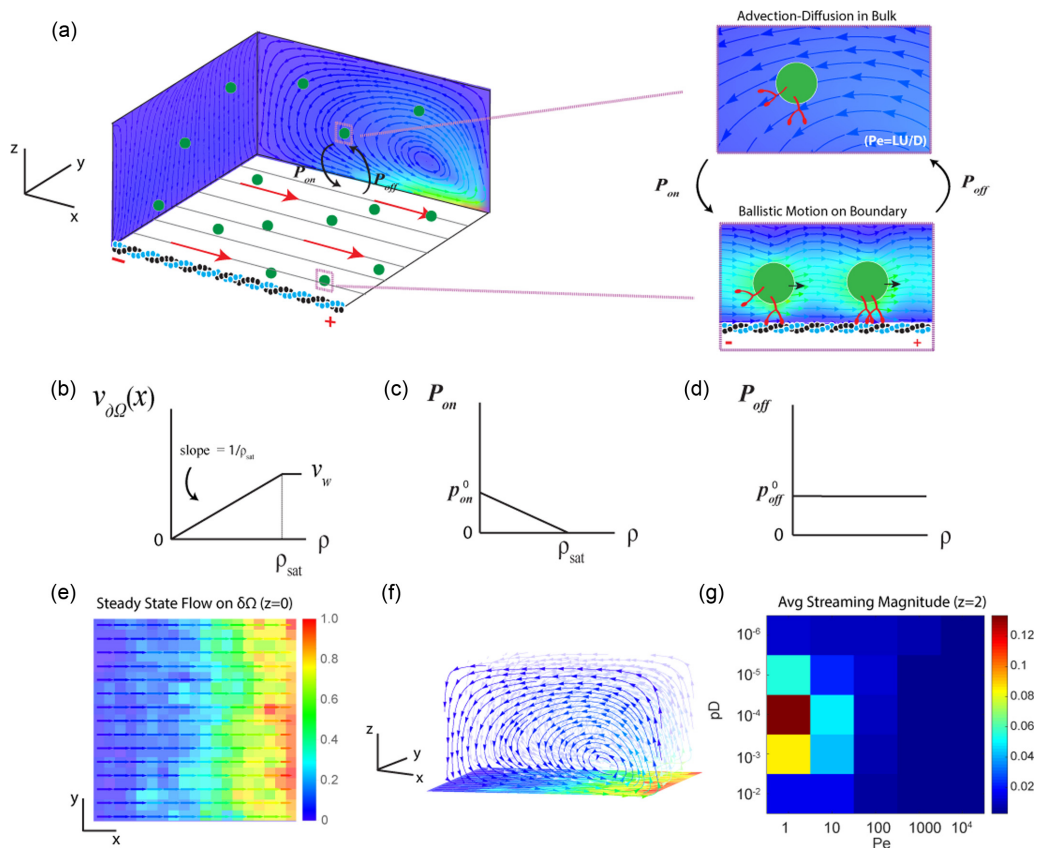


FIG. 2. Model for surface-driven flows in confined volumes. (a) Confined chamber of size $N_x \times N_y \times N_z = 20 \times 20 \times 10$ that consists of a single active surface at $z = 0$, uniformly coated with parallel and polarized actin filaments. The gray lines denote the orientation of particle trajectories on the surface. Active colloidal particles (green) bind and unbind from the surface with rates P_{on} and P_{off} . Bound particles walk ballistically in a fixed direction along the tracks, imparting momentum on the surrounding fluid and creating macroscopic flows. Unbound particles are free to advect and diffuse in the bulk, with relative strength set by the Péclet number Pe . (b) The velocity at each grid point $v_{\partial\Omega}(x)$ on the boundary increases linearly with particle concentration and saturates to the particle speed V . (c) The attachment rate P_{on} decreases linearly to zero at the saturating concentration ρ_{sat} , a value which is set by the grid and particle size, while (d) the detachment rate P_{off} is modeled as a constant. (e)–(g) Simulation results for a simple case: uniform flow in a closed chamber. All results are from snapshots of simulations recorded after simulating for 2×10^6 time steps to approach steady state, with each time step $dt \approx 10^{-6}L/V$ s. (e) The magnitude of the velocity at each point on the boundary for a specific choice of parameters [the optimum in (g)] shows an accumulation of particles toward the right edge of the chamber. The color bar depicts the flow magnitude on the surface, scaled by V to a maximum of one. (f) The existence of a wall forces the fluid at the edge upward, creating a 2D vortex in the xz plane. (g) Phase diagram of P_{off} and Pe , showing that high streaming velocities in a confined volume favor low Pe and an intermediate detachment rate. The average streaming velocity $\langle |u| \rangle / V$ is shown at $z/H = 0.2$ averaged in the x and y directions across the chamber. Here Pe is varied by changing D and keeping L and V constant. The P_{off} is reported in units of probability per time step.

dynamic viscosity of water, respectively) are fixed throughout our simulations, with $Re \sim 0$, well in the viscous regime. Unless explicitly mentioned otherwise, we report all results in the paper with nondimensionalized units $u^* = u/V$, $r^* = r/L$, and $t^* = t/(L/V)$ and for simplicity we drop the asterisks.

For typical values of both the motor speed V and the motor detachment rate P_{off} , there is a wide spectrum of biological variation. On the one hand, load-carrying myosin motors in *Chara corallina* can sustain fluid flows of speeds up to $100 \mu\text{m/s}$ over distances of a single cell that can be up to 10 cm long [21,22], whereas inside an oocyte the flows can be as small as $0.1 \mu\text{m/s}$ [15,69]. Thus, for an active particle with speed $V = 0.1\text{--}100 \mu\text{m/s}$ and radius $R = 0.1\text{--}1 \mu\text{m}$, in a microfluidic chamber of length $L \sim 100 \mu\text{m}$, the Péclet number ranges from $\text{Pe} \sim 1$ to 10^4 . On the other hand, the detachment rate P_{off} is related to the motor run length (also known as the processivity), which in our simulation corresponds to $\lambda = V/P_{\text{off}}$, with P_{off} having units of probability per time. For processive myosin motors, approximate run lengths can range between $\lambda = 100$ and 1000 nm [61–64], which yields a detachment rate of $P_{\text{off}} \sim 1\text{--}10 \text{ s}^{-1}$ (assuming a speed of $1 \mu\text{m/s}$). Engineered motors can reach processive run lengths approaching $10 \mu\text{m}$ [65], with multimotor complexes expected to reach even higher run lengths.

The above description gives us a range of parameters that are relevant for a motor-actuated system. For the entirety of the main text, unless otherwise mentioned, we set the length scales of our system at $L = 50 \mu\text{m}$ and $V = 1 \mu\text{m/s}$ and we use an active particle size of radius $R = 400 \text{ nm}$ (see Sec. II and Table I in [57] for an extended discussion on parameter choices and relating them to motor properties). To ensure convergence of our simulations, we use discretized time steps of $dt \approx 10^{-6}(L/V)$. We report rates with respect to discrete time steps. For instance, a detachment rate of $P_{\text{off}} = 1 \text{ s}^{-1}$ corresponds to $P_{\text{off}} \sim 10^{-4}$ per time step.

III. RESULTS

A. Optimal transport and flow topology

As a benchmark for us to compare our results in confinement, we first consider the simplest setup without any surface defects and periodic boundary conditions in x and y . A single active surface lies in the $z = 0$ plane with tracks aligned along x , and a glass slide sits with a no-slip condition at $z = H$. In this case, the uniform flow profile is $\mathbf{u} = u_{\text{max}}(z - H)\hat{x}$, where the maximum flow near the surface is $u_{\text{max}} = 2\langle u \rangle$ in terms of the average streaming magnitude $\langle u \rangle := \int u(z)dz/H = \phi V/2$ (Fig. S5 and movie S1 in [57]). This flow strength is directly determined by the motor speed V and the surface coverage fraction ϕ , which is set by the motor processivity. Thus, if we use highly processive and fast motors, the maximum flow speed near the surface can approach the motor speed itself, of order $u_{\text{max}} \sim 10\text{--}100 \mu\text{m/s}$, for the fastest natural cytoskeletal motors [22]. The engineered processive myosin motors [65] that are currently available are somewhat slower, up to $V \sim 10 \mu\text{m/s}$, but still capable of strong advection.

Next we consider a slightly more complex geometry: a closed rectangular chamber with one uniform active surface, as before, but with five no-slip surfaces [see Figs. 2(e) and 2(f) and movie S3 in [57]]. The steady state on the boundary for one particular choice of parameters shows an accumulation of particles at the right wall (at the plus end of the actin filaments) and a depletion of particles on the left [Fig. 2(e)]. The fluid at the right boundary is forced upward, creating a steady-state vortex in the xz plane [Fig. 2(f)]. Varying the Péclet number and detachment rates shows that higher streaming magnitudes occur for lower values of Pe and an intermediate value of P_{off} [Fig. 2(g) and Fig. S4 in [57]]. This optimum is explained as follows. On the one hand, attached particles will tend to accumulate at the chamber edges within a timescale $\tau_w \sim L/V$. Overly processive motors will therefore on average reach the opposite wall before they detach into the bulk, reducing the streaming velocity away from the edges. This sets a lower bound on the detachment probability, $\tau_{\text{detach}} = 1/P_{\text{off}} \leq \tau_w$, so we require that $P_{\text{off}} \geq V/L$ in order to establish nontrivial streaming velocities in confined volumes. On the other hand, particles that are not processive enough do not spend enough time on the surface to contribute significant momentum injection. A large diffusion coefficient (i.e., small Péclet number) helps to offset particle accumulation at edges and also homogenizes density fluctuations, which increases the streaming strength and stability, allowing for the establishment of steady-state flow structures (movies S2 and S3 in [57]). This is maximized in the limit $\text{Pe} \rightarrow 0$, when diffusion dominates advection, and motors spread through the box uniformly.

In summary, the flow velocity can be optimized with a high diffusivity and an intermediate processivity. Note that experimental realizations place constraints on these parameters, as discussed in Sec. II in [57]. We further note that the properties of the phase space diagram are particular to the geometry we have considered and other cases (such as periodic boundary conditions; see Fig. S5 in [57]) may yield very different results. Moreover, uniform motion in confined chambers will lead to recirculating streamlines that can transport particles in the \hat{z} direction, despite that activity on the surface is directed uniquely along \hat{x} [Fig. 2(f)]. Recirculation of streamlines due to the presence of defects in the surface is important when considering the design of fluid structures, which we do in later sections.

B. Light-modulated surfaces

One way to engineer different fluid structures would be to manipulate the orientation of tracks on a surface, an experimental perturbation made difficult by the fact that these tracks are often permanent when laid out. Instead, advances in optogenetics have enabled a simpler means of dynamic control via light. Engineered motors whose direction along an actin filament are switchable by light provide a mechanism to reprogram the same surface by changing how the motors interact with it [49]. We now explore this regime to see how we can program and pattern bulk flow with variable surface light patterns.

Consider the same active surface as in Fig. 2(a) with all tracks oriented in the \hat{x} direction. Suppose the $x > 0.5$ (right) half of the box is now illuminated, redirecting the optically controllable particles in that region toward the minus end [Figs. 3(a) and 3(c)]. We term the resulting structure the head-on defect, since now two populations of motile particles are walking into each other at a line defect formed by the light pattern. This gives rise to two distinct vortices on either side of the domain junction [Fig. 3(c)]. Similarly, we can also choose to illuminate the $y > 0.5$ half of the box, giving rise to a shear defect configuration [Figs. 3(b) and 3(d)]. On a surface patterned with uniformly oriented tracks, the head-on and shear defects are the two fundamental modes patterned by light.

These two flow structures have different properties that may be useful for different applications. Suppose, for example, that at subsequent stages of a chemical process two particle transport procedures are needed. Figures 3(e) and 3(f) show that the shear and head-on defects preferentially transport tracer particles in different directions. The head-on defect is most effective at spreading particles along the \hat{z} coordinate, as evidenced by the concentration profile of tracers initially in the bottom half of the box being spread uniformly along \hat{z} by the end of the simulation [Fig. 3(e)]. On the other hand, the shear defect is more effective at spreading along the \hat{y} coordinate [Fig. 3(f)]. Note that in both cases the direction of motion along the boundary is strictly in the \hat{x} direction; it is the geometry of the confined chamber (i.e., the location of walls and defects) that gives rise to recirculating streamlines.

A significant advantage of light-controlled surface patterning is the ease of transitioning from one flow structure to another. As a proof of principle, we conducted a simulation (see movie S4 in [57]) where we transition from a shear defect to a head-on defect and back to a shear defect again, with period 2×10^6 time steps, detachment rate $P_{\text{off}} = 10^{-4}$ per time step, and $\text{Pe} = 1$ [the optimum in Fig. 2(g)]. In our model, we assume that the behavior of the motile particles switches instantaneously with the external light perturbation. Figures 3(g) and 3(h) show that with each transition, the flow relaxes to its unique steady state for each boundary condition after a short relaxation time which is set by Pe . Interestingly, the shear defect generates a slightly lower streaming velocity despite having on average more particles attached to the boundary.

C. Systematic design of flow patterns in confined geometries

Next we consider the challenge of designing bulk flow patterns via surface activity and we consider the breadth of design space that is available. To speed up our simulations, we continue in the optimal limit $\text{Pe} \rightarrow 0$ where active particles cover all surfaces uniformly and simulate the steady-state flow structure in chambers of size $N_x \times N_y \times N_z = 40 \times 40 \times 40$. Hence, we no

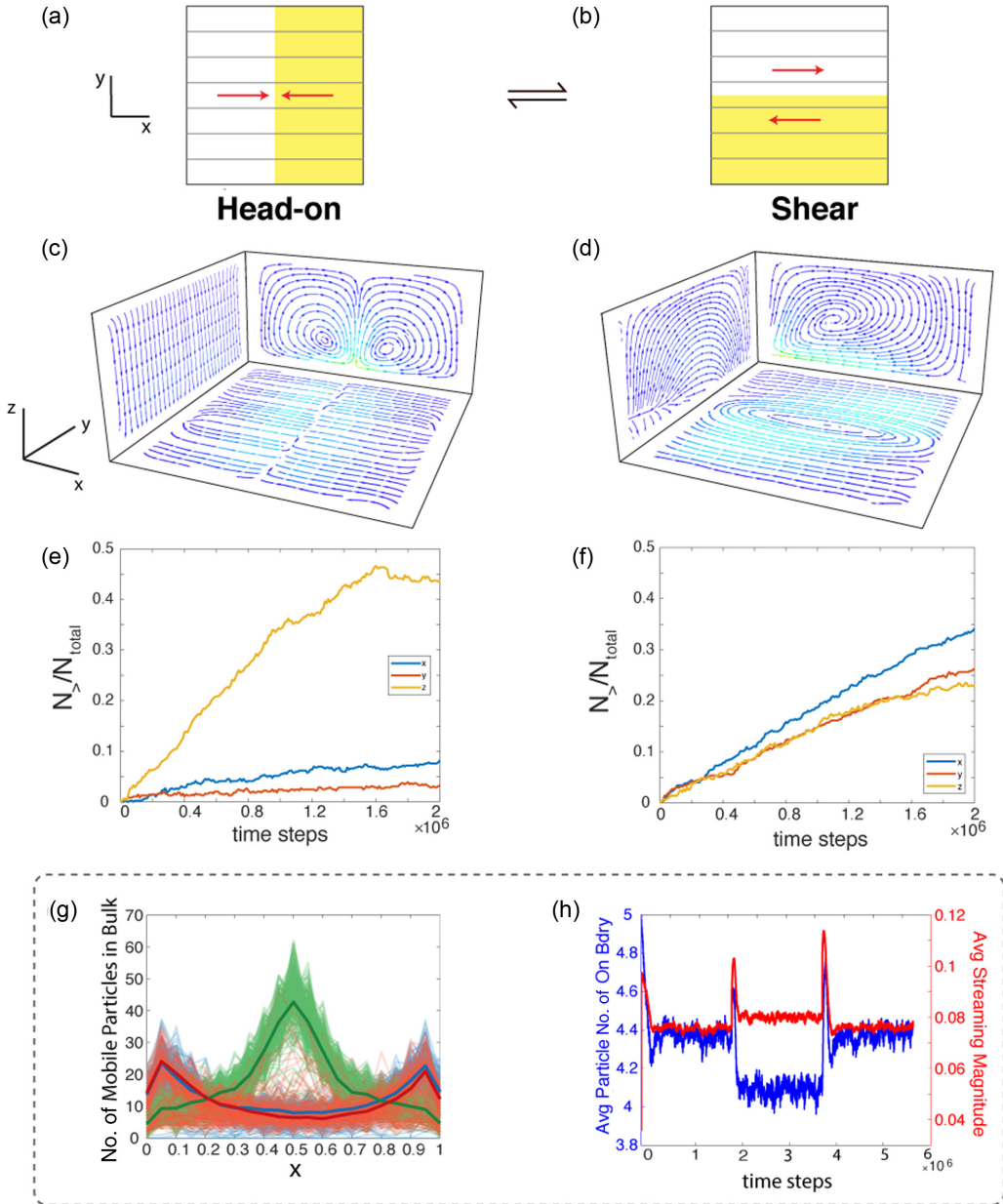


FIG. 3. Static and dynamic surface-patterned defects using light-controlled active colloidal particles in confined volumes. (a) and (b) Schematic of a light pattern on the $z = 0$ surface of a chamber with dimensions $N_x \times N_y \times N_z = 20 \times 20 \times 10$. In (a) the $x > 0.5$ half of the plane is illuminated by light and in (b) the $y > 0.5$ half is illuminated. (c) and (d) Resulting steady-state flow patterns. In (c) the line defect on the active surface at $x = 0.5$ causes fluid to be pushed upward, creating two distinct vortices. In (d) the line defect along $y = 0.5$ creates vortices of opposite chirality in distinct regions of the chamber ($y < 0.5$ and $y > 0.5$). Confinement of the fluid additionally gives rise to recirculating streamlines in the xy plane. (e) and (f) Head-on and shear defects preferentially mix passively advecting particles ($Pe_{\text{tracer}} = 10^4$) in different directions. Plotted on the y axis is the fraction of tracer particles in the initially empty portion of the box as a function of time. Here $N_>$ denotes the number of particles at $x, y, z > 0.5, 0.5, 0.25$ for each of the three curves, respectively. (e) For the head-on defect, particles are nearly evenly distributed between the $z < 0.25$ and $z > 0.25$ halves of the

longer simulate the particle dynamics explicitly and study the steady-state flow structures obtained by patterning surfaces directly with constant slip velocities. In reality, when Pe is nonzero, the magnitude of the flows will be more concentrated around defects (as shown in the previous section), but the streamlines will be similar (Fig. S4 in [57]). Though these surface velocities can be patterned arbitrarily, the resulting bulk flows must still obey the constraints set by the Stokes equations and incompressibility. The question arises how the optogenetic design can be optimized to alleviate those constraints in terms of transport and streamline connectivity.

For surface patterning, we utilize the language of defects that refer to zones where surface bound active particles dramatically change behavior. Starting with a single active surface with uniformly oriented filaments, different regions of left- or right-moving fluid can be created with light, as depicted for the head-on, shear, and patch defects [Figs. 4(a i), 4(a ii), and 4(a iii), respectively]. Again, all three patterns are interchangeable by dynamically changing the pattern of light. We can add an additional handle by no longer subjecting the filaments to be uniformly oriented. Alternating orthogonal patches of tracks, in tandem with a light pattern on the surface, can give rise to flow structures such as a vortex [Fig. 4(a iv)].

Integrated streamlines of the patch defect in Fig. 4(c i) highlights the separatrix formed by a small region of oppositely moving flow. Streamlines shown in red traverse clockwise and are centered on top of the patch, whereas all other streamlines travel counterclockwise. The head-on and patch defects therefore have a compartmentalizing effect, with regions of streamlines that do not mix. Conversely, Fig. 4(c ii) shows that the streamlines of the vortex defect traverse the xy plane as well as a distance of over half the height of the grid in z . The shear and vortex defects are therefore effective fluid mixers. These countervailing properties of compartmentalizing and mixing can guide the design of numerous functions useful in self-driven microfluidics.

We can further build upon the complexity of our designs by patterning multiple surfaces at once. Figure 4(b) approaches this systematically by considering only head-on [Figs. 4(b i), 4(b ii), and 4(b v) or shear defects [Figs. 4(b iii), 4(b iv), and 4(b vi)] on two or four surfaces. Interpreting the resultant flow structures created by head-on defects is straightforward: Two stable vortices will form on either side of a defect, where the flows move either toward ($\rightarrow \leftarrow$) or away ($\leftarrow \rightarrow$) from each other. Integrated streamlines of the flow field of Fig. 4(b v) in Fig. 4(c iii) show that the streamlines are two dimensional: Each of the eight vortex compartments remain unmixed in y . On the other hand, patterning with shear defects can lead to mixing within each compartment. Figure 4(b vi) depicts four consecutive active surfaces, with each pair of opposite faces patterned with shear defects of opposite signs ($\uparrow \downarrow$ and $\downarrow \uparrow$). In the xz plane, this gives rise to head-on defects at the four corners, creating four stable vortices. However, recirculation in the yz and xy planes cause the streamlines within the four vortices to traverse along the y coordinate, as depicted in Fig. 4(c iv).

The expectation that shear defects give rise to three-dimensional streamlines is a general but not very robust rule however. If one were to flip the signs of the velocity patterned on the two walls with surface normal to the x axis, the head-on defects at the corners would be eliminated, leading to a continuous current that runs counterclockwise in the $y < 0.5$ region of the box and clockwise in the other (Fig. S7 in [57]). Interestingly, the resulting streamlines are again coplanar.

←

FIG. 3. (Continued) box, but mostly remain in the $x < 0.5$ and $y < 0.5$ regions, showing that there is little mixing in x and y . (f) On the other hand, the shear defect is less effective at mixing in \hat{z} but is able to mix particles along \hat{y} due to recirculation. (g) and (h) An optically controllable system allows easy temporal switching from one flow structure to another. As a proof of principle, we switch between head-on and shear defects, with period 2×10^6 time steps and parameters $P_{\text{off}} = 10^{-4}$ and $Pe = 1$. (g) Distribution of motile particles, where time moves from blue to green to red. (h) Shown in red is the average streaming magnitude, computed as the spatially averaged fluid magnitude as a function of time, and in blue the average number of particles attached to the boundary as a function of time. Interestingly, the average streaming magnitude of the head-on defect is greater even though the number of attached particles on the boundary is slightly less than that of the shear defect.

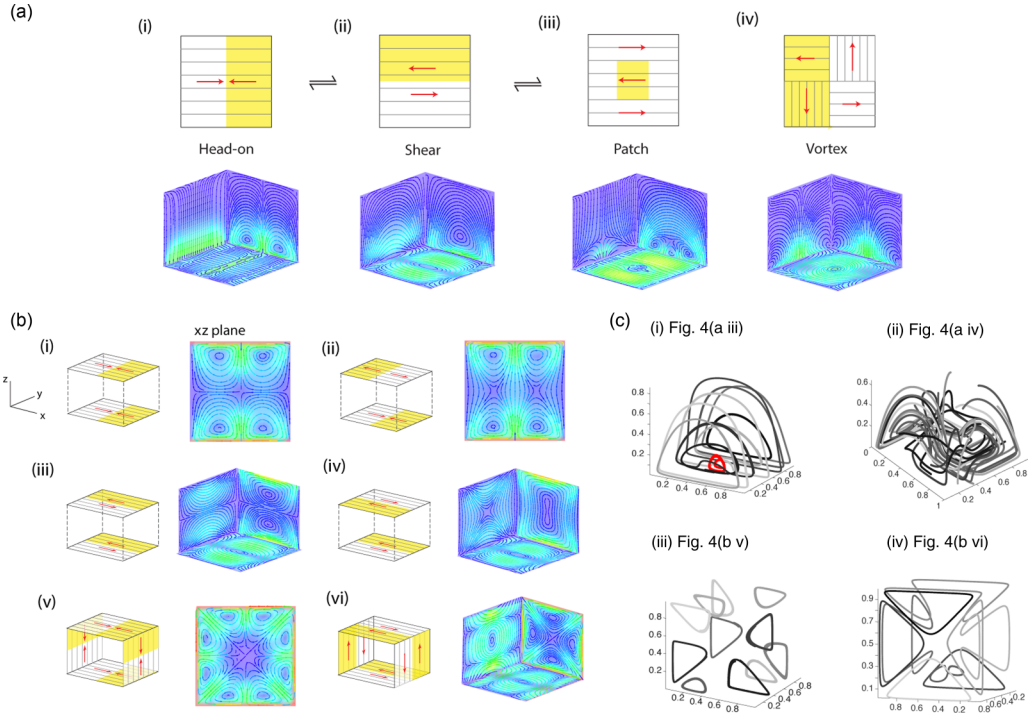


FIG. 4. Design space of surface-driven flows using mainly head-on and shear defects. All flow structures are solved on an $N_x \times N_y \times N_z = 40 \times 40 \times 40$ grid. (a) Each panel depicts a pattern of light on a single active boundary (top) and the corresponding 3D flow structure (bottom). Note that (i)–(iii) are interchangeable by light, whereas (iv) introduces additional complexity where the orientation of actin on the surface is no longer fully uniform. (b) Panels (i), (ii), and (v) pattern two or four surfaces with head-on defects. Since the resulting streamlines are effectively two dimensional, only xz cross sections of the flow structures are plotted. Panels (iii), (iv), and (vi) consider the same but with shear defects and with the full 3D flow structure to highlight the recirculating streamlines. (c) Select streamlines from (a) and (b) are plotted to enhance visualization of the flow structures. Note the red streamlines in (i), which highlights the particles trapped in the clockwise vortex established by the oppositely moving patch in Fig. 3(a iii). Contrasting (iii) with (iv) shows the effect of the recirculating streamlines: Particles in the former remain advected in the xz plane whereas particles in the latter circulate in xy .

Until now we have focused entirely on steady-state constant flows, harnessing only the spatial programming of light. We want to highlight the fact that temporal patterning opens up an even greater design space (movies S5 and S6 in [57]). Consider, for example, a continuous transition from a head-on to shear defect by smoothly varying the angle of the light pattern with the y axis (movie S5 in [57]). We can also assign an angular velocity to the light angle, generating a rotating light field. Although at low Reynolds numbers the fluid will relax instantaneously to the new boundary conditions, there is still a finite relaxation time associated with the redistribution of motile particles. In addition, the path taken by tracer patterns in a nonconstant Stokes fluid is not obvious. Further investigation into the effects and possible functionality of nonconstant flows is left for future work.

D. Interior squirmer model

Given the quickly increasing complexity of the resulting flows and the myriad possibilities of surface patterns, it is clear that adopting a more analytical approach to understanding the design space of boundary-driven flows is required. For this we turn to solutions of the squirmer model

on a sphere [60,70–73]. Initially adopted to study the external flow fields of microswimmers, we invert the problem and study instead the flow structure within the sphere [31–35,74], subject to the condition that flows normal to the surface vanish on the boundary. The resulting general solution for incompressible Stokes flow inside a sphere is given by

$$u_r(r, \theta, \phi) = \sum_{n=1}^{\infty} \sum_{m=0}^n n r^{n-1} P_n^m(\cos \theta) \left(1 - \frac{r^2}{R^2}\right) \quad (2)$$

$$\begin{aligned} & \times (b_{mn} \cos m\phi + \tilde{b}_{mn} \sin m\phi), \\ u_{\theta} = & \sum_{n=1}^{\infty} \sum_{m=0}^n r^{n+1} \sin \theta \hat{P}_n^m(\cos \theta) \left(\frac{n+3}{(n+1)R^2} - \frac{1}{r^2}\right) \\ & \times (b_{mn} \cos m\phi + \tilde{b}_{mn} \sin m\phi) \end{aligned} \quad (3)$$

$$\begin{aligned} & + \frac{mr^n}{\sin \theta} P_n^m(\cos \theta) (\tilde{c}_{mn} \cos m\phi - c_{mn} \sin m\phi), \\ u_{\phi} = & \sum_{n=1}^{\infty} \sum_{m=0}^n \frac{mr^{n+1} P_n^m(\cos \theta)}{\sin \theta} \left(\frac{1}{r^2} - \frac{(n+3)}{(n+1)R^2}\right) \\ & \times (\tilde{b}_{mn} \cos m\phi - b_{mn} \sin m\phi) \\ & + r^n \sin \theta \hat{P}_n^m(\cos \theta) (c_{mn} \cos m\phi + \tilde{c}_{mn} \sin m\phi), \end{aligned} \quad (4)$$

where $P_n^m(x)$ are the associated Legendre polynomials indexed by integers n and m , $\hat{P}_n^m(x) = \partial_x P_n^m(x)$ is its derivative, and the radius of the sphere is R . For the sake of simplicity we set $b_{mn} = \tilde{b}_{mn}$ and $c_{mn} = \tilde{c}_{mn}$, which fixes the phase of ϕ while keeping the topology the same. The modes are thus denoted by two variables b_{mn} and c_{mn} .

The first few axisymmetric modes are shown to match with the simulated flow structures on a grid (Fig. 5). We observe that the b modes are aligned longitudinally across the sphere, whereas the c modes run along lines of latitude and form closed streamlines. Cross sections of the box and sphere reveal the similarities between the internal flow structures. The topological equivalence between a sphere and a box dictates that these flow structures should be compatible. We do note, however, that corner effects can give rise to eddies that are unique to the geometry of a box [75]. Most interestingly, the b_{20} and c_{20} modes have built-in defects analogous to topologies proposed earlier: The former consists of a line of head-on defects at the equator, while the latter consists of two oppositely rotating hemispheres, giving rise to a shear defect along the equator. The spherical solutions therefore present a natural framework in which to embed the design space of surface-driven flow structures.

Plots of higher-order modes and their streamlines [Fig. 6(a) and Figs. S8–S12 in [57]] show that these general rules of thumb still apply: b modes give rise to patches of oppositely moving flow on the surface, while c modes give rise to closed vortices. Higher-order modes give rise to more patches or more vortices, corresponding to smaller compartments in which tracer particles can traverse (Figs. S11 and S12 in [57]). The b modes are better at mixing particles radially within their compartments due to streamlines that redirect particles toward the $z = 0$ axis, whereas particles move along concentric closed curves at approximately constant radius in c modes (Figs. S8–S10 in [57]). These properties can be combined and used when designing microfluidic devices that require specific bulk flow patterns.

E. Chaotic mixing by mode superposition

Inspired by previous work showing that Stokes flows within droplets can give rise to chaotic streamlines [76–79], we ask whether our surface-driven flow patterns can do the same. Whereas the individual b and c modes do not feature chaos, we do find evidence of chaotic mixing in superpositions of these modes (Fig. 6). To quantify this, we consider the trajectories of tracer particle

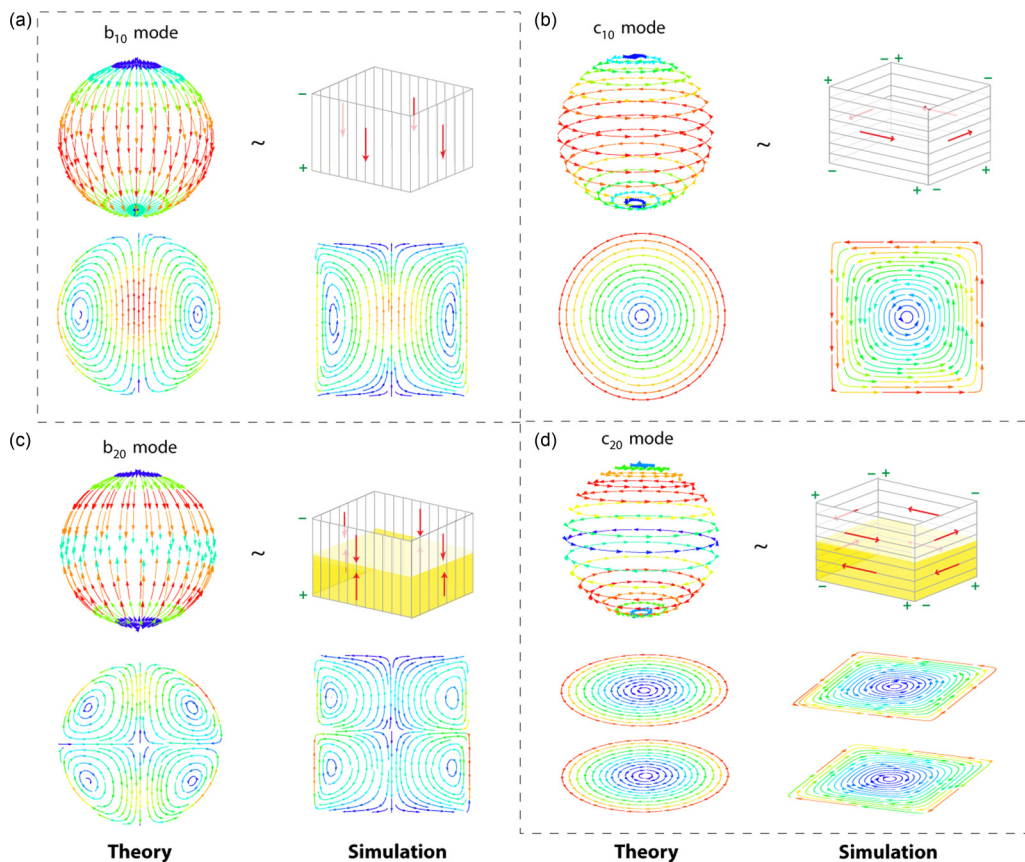


FIG. 5. Fundamental modes of the squirmer model: an analytical approach to boundary-driven flows. (a)–(d) Comparisons between theory (left) and simulations (right) for the first four axisymmetric modes. The green \pm symbols at the corners of the box indicate the polarity of the actin filaments patterned on the boundary. The top row of each panel depicts the surface patterning and the bottom row depicts the internal flow structures taken at some cross section. (a) and (c) The surface patterns of the b_{10} and b_{20} modes lie on longitudinal tracks. The b_{10} mode consists of uniform (in direction) motion from the north to the south pole, while the b_{20} mode naturally encodes a line of head-on defects at the equator. All interior flow structures are taken at the cross section $y = 0$. (b) and (d) Conversely, the surface patterns of the c_{10} and c_{20} modes lie on lines of latitude. Similar to the b_{20} mode, the c_{20} mode naturally encodes a shear defect along its equator. The interior cross sections of c_{10} for both the sphere and the box are taken at $x = 0$, while the pair of cross sections of c_{20} are taken at $\theta = \pi/3, 3\pi/4$ for the sphere and at $z = 0.25, 0.75$. Cross sections of the sphere and box in all four panels show that the interior flow structures are analogous. This shows that the language of head-on and shear defects is intrinsically built into the squirmer model.

pairs that are initially spaced a distance $dr_0 = 10^{-6}$ apart (in dimensionless units). Figure 6(b) depicts ten such trajectories subject to the b_{21} flow field only. The blue circles denote the starting positions of one pair of particles, which cannot be visually resolved. The green circles denote their final positions after integrating to time $t = 500$. The red curve in Fig. 6(f) plots the separation dr as a function of time, averaged over 1000 randomly seeded trajectories, and shows that the particle pairs remain close together throughout their trajectories, with a final separation less than $dr = 10^{-3}$. Similarly, the blue curve in Fig. 6(f) suggests that the c_{21} mode is also not chaotic.

Trajectories of the $b_{21} + c_{21}$ modes combined, however, will on average diverge rapidly to a distance comparable to the system size ($R = 1$). Figure 6(c) depicts a single pair of trajectories

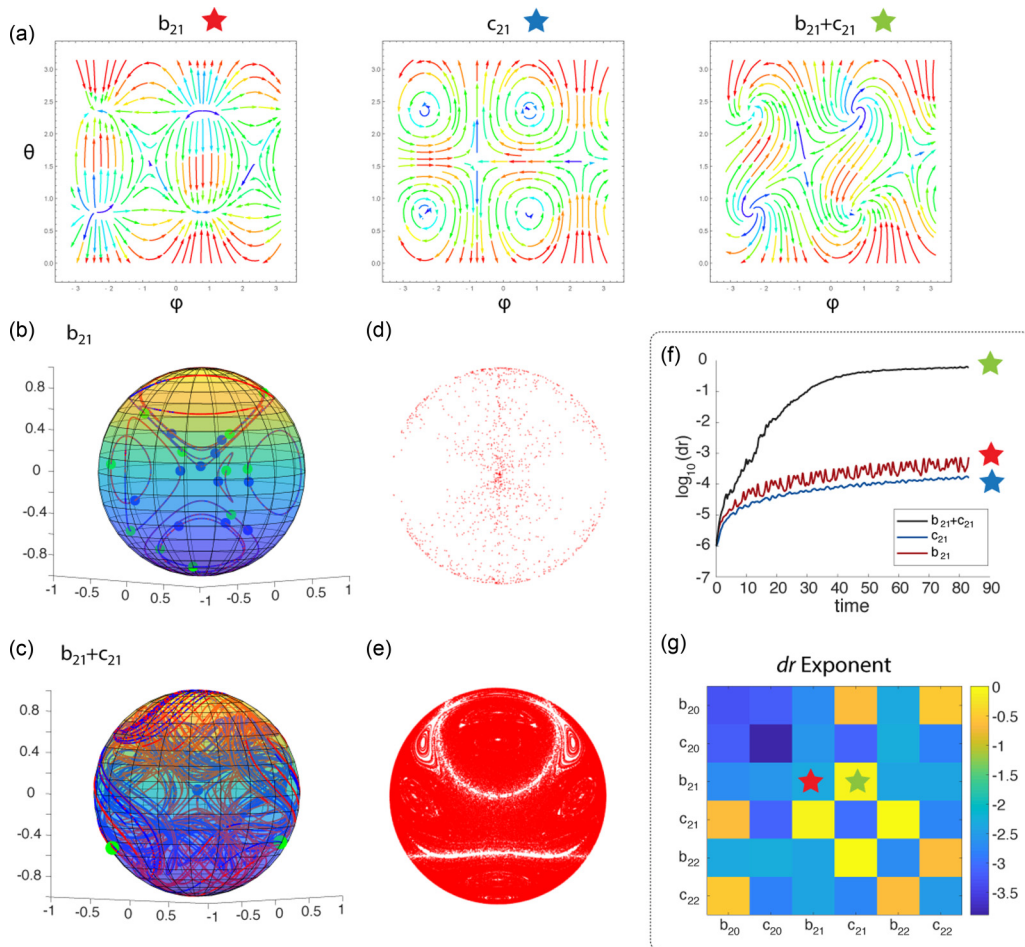


FIG. 6. Emergence of chaotic mixing. (a) Surface streamline structure of the modes (i.e., the fluid velocity at $r/R = 1$) plotted as a function of the spherical angles θ and ϕ . Note that the b modes give rise to patches of oppositely moving flow, whereas the c modes comprise closed vortices. (b) Examples of ten separate trajectories of the b_{21} mode. The blue circles denote the starting points of two particles, spaced $dr/R = 10^{-6}$ apart, a distance that cannot be resolved by eye. The green circles denote the ending positions after integrating for $t = 500$, which are still very closely spaced, showing that the two trajectories do not substantially diverge. (c) Example of a single chaotic trajectory of the $b_{21} + c_{21}$ mode. Note the positions of the green circles, which now span a distance comparable to the size of the droplet. (d) Poincaré section at $x = 0$ for the b_{21} mode computed from 1000 trajectories. Note that the plane is only sparsely populated. (e) The Poincaré section of $b_{21} + c_{21}$, on the other hand, nearly fills the entire plane. (f) Evolution in time of the logarithmic displacement between pairs of particles initially spaced $dr/R = 10^{-6}$ apart, averaged over 1000 randomly seeded trajectories. These plots show that of the three modes in (a), only the superposed mode shows evidence of chaotic mixing on the scale of the droplet size. (g) Exponents of the time evolution of dr after integrating for $t = 500$ for various superpositions of modes, indicated by the row r and column c of the element in the matrix. For example, $(r, c) = (2, 3)$ denotes the $c_{21} + b_{22}$ mode. The matrix shows that the only modes that show evidence of chaotic mixing are the b and c superposed modes. However, not all such modes are chaotic, as evidenced by the $b_{21} + c_{22}$ mode.

that begin at the blue circle near the center of the sphere. After a time $t = 500$, the green circles show the separation of these two particles at a distance comparable to the sphere diameter. This chaotic mixing is further illustrated by the Poincaré sections at $x = 0$ for the b_{21} and $b_{21} + c_{21}$ modes [Figs. 6(d) and 6(f)], each built from 1000 randomly seeded trajectories. The Poincaré section of b_{21} is notably sparser than that of $b_{21} + c_{21}$, showing that the superposition of modes is far more effective at mixing.

To understand this better, we map out the entire phase space of mixing potential by superpositions of the $n = 2$ modes [Fig. 6(g)]. This heat map shows the exponent of dr for each pair of superposed modes. Only the modes consisting of b superposed onto c lead to chaotic advection, suggesting that fundamental properties from each mode are necessary ingredients. Somewhat surprisingly, the axisymmetric mode b_{20} showed moderate signs of mixing when superposed with the c_{21} and c_{22} modes, but the $b_{21} + c_{22}$ mode combination did not. Though we can predict the flow structures of simple surface patterns, it is not obvious which of the more complex topologies will lead to chaotic mixing and which do not. Prior theoretical work has shown that fluid properties such as stretching, twisting, and folding are essential for chaotic mixing [76,77,79–81].

Moreover, we have also examined the effect of Brownian motion on top of chaotic mixing (see Fig. S13 in [57]). These results show that chaotic flows always significantly reduce the mixing time, up to tens of times faster than nonchaotic flows and orders of magnitude faster than diffusion alone, for sufficiently large chambers or sufficiently fast flows.

IV. DISCUSSION

In this paper we have proposed a class of flow patterns that utilize surface-driven flows rather than externally applied pressure gradients in confined geometries. We first considered a realization of such active boundaries using a suspension of light-controllable molecular motors. These particles can bind to directional tracks grafted onto the surfaces of a microfluidic chamber, and hence generate surface-driven flows. We demonstrated that these currents can be optimized by tuning the motor processivity and the motor velocity. This nonequilibrium transport was augmented further by optogenetic perturbations, whereby the same active surface can be reprogrammed to generate a myriad of different flow structures. We then generalized the problem of designing fluid structures by moving from numerical to analytical analysis, embedding the language of our surface patterns in terms of the squirmer modes. Different classes of topological defects created by light patterning give rise to flow structures that each have different functions, such as hydrodynamic compartmentalization, translation and rotation, and chaotic mixing.

Importantly, the concept of active boundaries is much more general than any specific implementation. That is, besides molecular motors, surface-driven flow structures may equally be driven by other microfluidic technologies, and fluid design concepts have been developed for these systems as well [[15,21–23,25–39,41,42],[44]]. For example, artificial cilia [25–30] could also be used to create a patterned active surface, but dynamic local control cannot be achieved since the ciliary patterning cannot be moved once established, and miniaturization remains a challenge. Phoretic pumps [31–35], where a surface is coated with fixed patches of chemical catalysts, also suffer from a lack of dynamic control. Additionally, the chemicals used (typically H_2O_2) may not be biocompatible or interfere with other desired laboratory-on-a-chip reactions. Induced-charge electrokinetics is another important means of creating boundary-driven flows by applying an electric field to an ionic solvent [82,83], which has proved to be effective in many microfluidic applications including chaotic mixing. However, similar to the artificial cilia and phoretic pumps, the electrodes are fixed in place, and the high voltages used can affect sensitive biochemistry near the electrodes.

Another key advantage of a microfluidic system driven by molecular motors is that the active particles are *coupled*, rather than permanently attached, to the boundary. A region of the boundary will not be active unless a motor binds to it. Thus, the activity at a local patch of the boundary is dependent on the local concentration centered on that patch. Therefore, the energy consumption can be localized to a region of the surface by concentrating particles (i.e., with a head-on defect)

and thus concentrating activity. Moreover, while we focused on controlling active particles in one direction, multiple channels can be combined to enable full orthogonal control of the active carpet. For example, myosin motors tuned by one wavelength of light can generate surface flows via actin tracks along the x direction, while kinesins tuned by a different wavelength of light can walk on microtubules grafted along y .

The generality of the concept of surface-driven flows led us to develop an analytic theory that reveals the possible flow structures in terms of fundamental modes, which may be superposed spatiotemporally. Switching dynamically from one mode to another enables the generation of multiple flow structures from a single active surface, without the need for physical channel fabrication. The simplicity of such a microfluidic design platform is the minimal amount of experimental manipulation required during operation. Hence, highly complex and dynamic time-varying protocols may be designed with these internally driven flows. It would be very interesting in the future to ask whether or not these units can be used to create logic gates [13,84], microfluidic assembly lines [47], or for other applications such as sorting particles of difference sizes [85]. Instead of spherical active particles that move along the surface, one could also consider active filaments [86,87]. Overall, this platform provides a fertile testing ground for understanding and designing active carpets from first principles.

ACKNOWLEDGMENTS

We acknowledge P. Ruijgrok for many helpful discussions throughout this project and for detailed comments on the final manuscript. This work was supported by funding from the National Science Foundation Center for Cellular Construction (NSF Grant No. DBI-1548297), the U.S. Department of Agriculture (USDA-NIFA AFRI Grants No. 2020-67017-30776 and No. 2020-67015-32330), a Human Frontier Science Program Fellowship to A.J.T.M.M. (Grant No. LT001670/2017), NSF Grant No. DMR-1905675, NIH Grant No. R01 GM114627 to Z.B., NSF Career Award 1453190 and Schmidt Innovation Fellowship to MP, and a grant from the W. M. Keck Foundation to M.P. and Z.B.

-
- [1] S. Ramaswamy, The mechanics and statistics of active matter, *Annu. Rev. Condens. Matter Phys.* **1**, 323 (2010).
 - [2] M. C. Marchetti, J. F. Joanny, S. Ramaswamy, T. B. Liverpool, J. Prost, M. Rao, and R. A. Simha, Hydrodynamics of soft active matter, *Rev. Mod. Phys.* **85**, 1143 (2013).
 - [3] A. Doostmohammadi, J. Ignés-Mullol, J. M. Yeomans, and F. Sagués, Active nematics, *Nat. Commun.* **9**, 3246 (2018).
 - [4] D. Needleman and Z. Dogic, Active matter at the interface between materials science and cell biology, *Nat. Rev. Mater.* **2**, 17048 (2017).
 - [5] T. Vicsek, A. Czirók, E. Ben-Jacob, I. Cohen, and O. Shochet, Novel Type of Phase Transition in a System of Self-Driven Particles, *Phys. Rev. Lett.* **75**, 1226 (1995).
 - [6] A. Cavagna, A. Cimarelli, I. Giardina, G. Parisi, R. Santagati, F. Stefanini, and M. Viale, Scale-free correlations in starling flocks, *Proc. Natl. Acad. Sci. USA* **107**, 11865 (2010).
 - [7] J. Toner, Y. Tu, and S. Ramaswamy, Hydrodynamics and phases of flocks, *Ann. Phys. (NY)* **318**, 170 (2005).
 - [8] O. Sliusarenko, D. R. Zusman, and G. Oster, Aggregation during fruiting body formation in *Myxococcus xanthus* is driven by reducing cell movement, *J. Bacteriol.* **189**, 611 (2007).
 - [9] Y. Wu, A. D. Kaiser, Y. Jiang, and M. S. Alber, Periodic reversal of direction allows Myxobacteria to swarm, *Proc. Natl. Acad. Sci. USA* **106**, 1222 (2009).
 - [10] S. Thutupalli, M. Sun, F. Bunyak, K. Palaniappan, and J. W. Shaevitz, Directional reversals enable *Myxococcus xanthus* cells to produce collective one-dimensional streams during fruiting-body formation, *J. R. Soc. Interface* **12**, 20150049 (2015).

- [11] H. H. Wensink, J. Dunkel, S. Heidenreich, K. Drescher, R. E. Goldstein, H. Löwen, and J. M. Yeomans, Meso-scale turbulence in living fluids, *Proc. Natl. Acad. Sci. USA* **109**, 14308 (2012).
- [12] A. J. T. M. Mathijssen, J. Culver, M. S. Bhmla, and M. Prakash, Collective intercellular communication through ultra-fast hydrodynamic trigger waves, *Nature (London)* **571**, 560 (2019).
- [13] F. G. Woodhouse and J. Dunkel, Active matter logic for autonomous microfluidics, *Nat. Commun.* **8**, 15169 (2017).
- [14] F. G. Woodhouse and R. E. Goldstein, Spontaneous Circulation of Confined Active Suspensions, *Phys. Rev. Lett.* **109**, 168105 (2012).
- [15] R. E. Goldstein, I. Tuval, and J.-W. van de Meent, Microfluidics of cytoplasmic streaming and its implications for intracellular transport, *Proc. Natl. Acad. Sci. USA* **105**, 3663 (2008).
- [16] T. D. Ross, H. J. Lee, Z. Qu, R. A. Banks, R. Phillips, and M. Thomson, Controlling organization and forces in active matter through optically defined boundaries, *Nature (London)* **572**, 224 (2019).
- [17] F. Guzmán-Lastra, H. Löwen, and A. J. T. M. Mathijssen, Active carpets drive non-equilibrium diffusion and enhanced molecular fluxes, *Nat. Commun.* **12**, 1906 (2021).
- [18] X. M. Bustamante-Marin and L. E. Ostrowski, Cilia and mucociliary clearance, *CSH Persp. Biol.* **9**, a028241 (2017).
- [19] J. Elgeti and G. Gompper, Emergence of metachronal waves in cilia arrays, *Proc. Natl. Acad. Sci. USA* **110**, 4470 (2013).
- [20] G. R. Ramirez-San Juan, A. J. T. M. Mathijssen, Mu He, L. Jan, W. Marshall, and M. Prakash, Multi-scale spatial heterogeneity enhances particle clearance in airway ciliary arrays, *Nat. Phys.* **16**, 958 (2020).
- [21] N. S. Allen and R. D. Allen, Cytoplasmic streaming in green plants, *Annu. Rev. Biophys. Bioeng.* **7**, 497 (1978).
- [22] R. Goldstein and J. Meent, A physical perspective on cytoplasmic streaming, *Interface Focus* **5**, 20150030 (2015).
- [23] F. G. Woodhouse and R. E. Goldstein, Cytoplasmic streaming in plant cells emerges naturally by microfilament self-organization, *Proc. Natl. Acad. Sci. USA* **110**, 14132 (2013).
- [24] K. Wolff, D. Marenduzzo, and M. E. Cates, Cytoplasmic streaming in plant cells: The role of wall slip, *J. R. Soc. Interface* **9**, 1398 (2012).
- [25] F. Fahrni, M. W. J. Prins, and L. J. van IJzendoorn, Micro-fluidic actuation using magnetic artificial cilia, *Lab Chip* **9**, 3413 (2009).
- [26] M. Vilfan, A. Potočnik, B. Kavčič, N. Osterman, I. Poberaj, A. Vilfan, and D. Babič, Self-assembled artificial cilia, *Proc. Natl. Acad. Sci. USA* **107**, 1844 (2010).
- [27] N. Coq, A. Bricard, F.-D. Delapierre, L. Malaquin, O. du Roure, M. Fermigier, and D. Bartolo, Collective Beating of Artificial Microcilia, *Phys. Rev. Lett.* **107**, 014501 (2011).
- [28] E. Milana, B. Gorissen, S. Peerlinck, M. De Volder, and D. Reynaerts, Artificial soft cilia with asymmetric beating patterns for biomimetic low-Reynolds-number fluid propulsion, *Adv. Funct. Mater.* **29**, 1900462 (2019).
- [29] H. Gu, Q. Boehler, H. Cui, E. Secchi, G. Savorana, C. De Marco, S. Gervasoni, Q. Peyron, T.-Y. Huang, S. Pane *et al.*, Magnetic cilia carpets with programmable metachronal waves, *Nat. Commun.* **11**, 2637 (2020).
- [30] A. F. Demirörs, S. Aykut, S. Ganzeboom, Y. A. Meier, R. Hardeman, J. de Graaf, A. J. T. M. Mathijssen, E. Poloni, J. A. Carpenter, C. Ünlü, and D. Zenhäusern, Amphibious transport of fluids and solids by soft magnetic carpets, *Adv. Sci.* **8**, 2102510 (2021).
- [31] S. Michelin, T. D. Montenegro-Johnson, G. De Canio, N. Lobato-Dauzier, and E. Lauga, Geometric pumping in autophoretic channels, *Soft Matter* **11**, 5804 (2015).
- [32] M. Lisicki, S. Michelin, and E. Lauga, Phoretic flow induced by asymmetric confinement, *J. Fluid Mech.* **799**, R5 (2016).
- [33] M. Shen, F. Ye, R. Liu, K. Chen, M. Yang, and M. Ripoll, Chemically driven fluid transport in long microchannels, *J. Chem. Phys.* **145**, 124119 (2016).
- [34] S. Michelin and E. Lauga, A reciprocal theorem for boundary-driven channel flows, *Phys. Fluids* **27**, 111701 (2015).

- [35] S. Michelin and E. Lauga, Universal optimal geometry of minimal phoretic pumps, *Sci. Rep.* **9**, 10788 (2019).
- [36] A. Bricard, J.-B. Caussin, D. Das, C. Savoie, V. Chikkadi, K. Shitara, O. Chepizhko, F. Peruani, D. Saintillan, and D. Bartolo, Emergent vortices in populations of colloidal rollers, *Nat. Commun.* **6**, 7470 (2015).
- [37] C. Bechinger, R. Di Leonardo, H. Löwen, C. Reichhardt, G. Volpe, and G. Volpe, Active particles in complex and crowded environments, *Rev. Mod. Phys.* **88**, 045006 (2016).
- [38] A. Zöttl and H. Stark, Emergent behavior in active colloids, *J. Phys.: Condens. Matter* **28**, 253001 (2016).
- [39] C. C. Maass, C. Krüger, S. Herminghaus, and C. Bahr, Swimming droplets, *Annu. Rev. Condens. Matter Phys.* **7**, 171 (2016).
- [40] C. Jin, Y. Chen, C. C. Maass, and A. J. T. M. Mathijssen, Collective Entrainment and Confinement Amplify Transport by Schooling Microswimmers, *Phys. Rev. Lett.* **127**, 088006 (2021).
- [41] N. Darnton, L. Turner, K. Breuer, and H. C. Berg, Moving fluid with bacterial carpets, *Biophys. J.* **86**, 1863 (2004).
- [42] A. J. T. M. Mathijssen, F. Guzmán-Lastra, A. Kaiser, and H. Löwen, Nutrient Transport Driven by Microbial Active Carpets, *Phys. Rev. Lett.* **121**, 248101 (2018).
- [43] X. Jin and I. H. Riedel-Kruse, Biofilm lithography enables high-resolution cell patterning via optogenetic adhesion expression, *Proc. Natl. Acad. Sci. USA* **115**, 3698 (2018).
- [44] L. E. Scriven and C. V. Sterling, On cellular convection driven by surface-tension gradients: Effects of mean surface tension and surface viscosity, *J. Fluid Mech.* **19**, 321 (1964).
- [45] V. Schaller, C. Weber, C. Semmrich, E. Frey, and A. R. Bausch, Polar patterns of driven filaments, *Nature (London)* **467**, 73 (2010).
- [46] P. S. Dittrich and A. Manz, Lab-on-a-chip: Microfluidics in drug discovery, *Nat. Rev. Drug Discov.* **5**, 210 (2006).
- [47] T. M. Schneider, S. Mandre, and M. P. Brenner, Algorithm for a Microfluidic Assembly Line, *Phys. Rev. Lett.* **106**, 094503 (2011).
- [48] M. Nakamura, L. Chen, S. C. Howes, T. D. Schindler, E. Nogales, and Z. Bryant, Remote control of myosin and kinesin motors using light-activated gearshifting, *Nat. Nanotechnol.* **9**, 693 (2014).
- [49] P. V. Ruijgrok, R. P. Ghosh, S. Zemsky, M. Nakamura, R. Gong, L. Ning, R. Chen, V. T. Vachharajani, A. E. Chu, N. Anand *et al.*, Optical control of fast and processive engineered myosins in vitro and in living cells, *Nat. Chem. Biol.* **17**, 540 (2021).
- [50] L. Huang, P. Manandhar, K.-E. Byun, P. B. Chase, and S. Hong, Selective assembly and alignment of actin filaments with desired polarity on solid substrates, *Langmuir* **22**, 8635 (2006).
- [51] L. Limberis, J. J. Magda, and R. J. Stewart, Polarized alignment and surface immobilization of microtubules for kinesin-powered nanodevices, *Nano Lett.* **1**, 277 (2001).
- [52] T. B. Brown and W. O. Hancock, A polarized microtubule array for kinesin-powered nanoscale assembly and force generation, *Nano Lett.* **2**, 1131 (2002).
- [53] G. Tsiavalariis, S. Fujita-Becker, and D. J. Manstein, Molecular engineering of a backwards-moving myosin motor, *Nature (London)* **427**, 558 (2004).
- [54] L. Chen, M. Nakamura, T. D. Schindler, D. Parker, and Z. Bryant, Engineering controllable bidirectional molecular motors based on myosin, *Nat. Nanotechnol.* **7**, 252 (2012).
- [55] N. Kumar, R. Zhang, J. J. De Pablo, and M. L. Gardel, Tunable structure and dynamics of active liquid crystals, *Sci. Adv.* **4**, eaat7779 (2018).
- [56] R. Zhang, S. A. Redford, P. V. Ruijgrok, N. Kumar, A. Mozaffari, S. Zemsky, A. R. Dinner, V. Vitelli, Z. Bryant, M. L. Gardel *et al.*, Spatiotemporal control of liquid crystal structure and dynamics through activity patterning, *Nat. Mater.* **20**, 875 (2021).
- [57] See Supplemental Material at <http://link.aps.org/supplemental/10.1103/PhysRevFluids.6.123104> for details.
- [58] A. Prosperetti and G. Tryggvason, *Computational Methods for Multiphase Flow* (Cambridge University Press, Cambridge, 2009).
- [59] M. J. Lighthill, On the squirming motion of nearly spherical deformable bodies through liquids at very small Reynolds numbers, *Comm. Pure Appl. Math.* **5**, 109 (1952).

- [60] J. R. Blake, A spherical envelope approach to ciliary propulsion, *J. Fluid Mech.* **46**, 199 (1971).
- [61] R. S. Rock, S. E. Rice, A. L. Wells, T. J. Purcell, J. A. Spudich, and H. L. Sweeney, Myosin vi is a processive motor with a large step size, *Proc. Natl. Acad. Sci. USA* **98**, 13655 (2001).
- [62] T. Sakamoto, F. Wang, S. Schmitz, Y. Xu, Q. Xu, J. E. Molloy, C. Veigel, and J. R. Sellers, Neck length and processivity of myosin V, *J. Biol. Chem.* **278**, 29201 (2003).
- [63] G. Cappello, P. Pierobon, C. Symonds, L. Busoni, J. Christof, M. Gebhardt, M. Rief, and J. Prost, Myosin V stepping mechanism, *Proc. Natl. Acad. Sci. USA* **104**, 15328 (2007).
- [64] M. Tominaga, H. Kojima, E. Yokota, H. Orii, R. Nakamori, E. Katayama, M. Anson, T. Shimmen, and K. Oiwa, Higher plant myosin XI moves processively on actin with 35 nm steps at high velocity, *EMBO J.* **22**, 1263 (2003).
- [65] T. D. Schindler, L. Chen, P. Lebel, M. Nakamura, and Z. Bryant, Engineering myosins for long-range transport on actin filaments, *Nat. Nanotechnol.* **9**, 33 (2014).
- [66] A. J. T. M. Mathijssen, A. Doostmohammadi, J. M. Yeomans, and T. N. Shendruk, Hydrodynamics of microswimmers in films, *J. Fluid Mech.* **806**, 35 (2016).
- [67] J. R. Blake, A note on the image system for a Stokeslet in a no-slip boundary, *Math. Proc. Cambridge* **70**, 303 (1971).
- [68] N. Liron and S. Mochon, Stokes flow for a stokeslet between two parallel flat plates, *J. Eng. Math.* **10**, 287 (1976).
- [69] M. E. Quinlan, Cytoplasmic streaming in the *Drosophila* oocyte, *Annu. Rev. Cell Develop. Biol.* **32**, 173 (2016).
- [70] S. Y. Reigh, L. Zhu, F. Gallaire, and E. Lauga, Swimming with a cage: Low-Reynolds-number locomotion inside a droplet, *Soft Matter* **13**, 3161 (2017).
- [71] T. J. Pedley, Spherical squirmers: Models for swimming micro-organisms, *IMA J. Appl. Math.* **81**, 488 (2016).
- [72] O. S. Pak and E. Lauga, Generalized squirming motion of a sphere, *J. Eng. Math.* **88**, 1 (2014).
- [73] F. Fadda, J. J. Molina, and R. Yamamoto, Dynamics of a chiral swimmer sedimenting on a flat plate, *Phys. Rev. E* **101**, 052608 (2020).
- [74] J. Happel and H. Brenner, *Low Reynolds Number Hydrodynamics* (Springer Netherlands, Dordrecht, 1983).
- [75] J. Dauparas and E. Lauga, Leading-order Stokes flows near a corner, *IMA J. Appl. Math.* **83**, 590 (2018).
- [76] K. Bajer and H. K. Moffatt, On a class of steady confined Stokes flows with chaotic streamlines, *J. Fluid Mech.* **212**, 337 (1990).
- [77] H. A. Stone, A. Nadim, and S. H. Strogatz, Chaotic streamlines inside drops immersed in steady Stokes flows, *J. Fluid Mech.* **232**, 629 (1991).
- [78] H. Aref, The development of chaotic advection, *Phys. Fluids* **14**, 1315 (2002).
- [79] T. Ward and G. M. Homsy, Chaotic streamlines in a translating drop with a uniform electric field, *J. Fluid Mech.* **547**, 215 (2006).
- [80] L. D. Smith, P. B. Umbanhowar, R. M. Lueptow, and J. M. Ottino, The geometry of cutting and shuffling: An outline of possibilities for piecewise isometries, *Phys. Rep.* **802**, 1 (2019).
- [81] J. M. Ottino and J. M. Ottino, *The Kinematics of Mixing: Stretching, Chaos, and Transport* (Cambridge University Press, Cambridge, 1989), Vol. 3.
- [82] T. M. Squires, Induced-charge electrokinetics: Fundamental challenges and opportunities, *Lab Chip* **9**, 2477 (2009).
- [83] M. Z. Bazant and T. M. Squires, Induced-charge electrokinetic phenomena, *Curr. Opin. Colloid Interf. Sci.* **15**, 203 (2010).
- [84] M. Prakash and N. Gershenfeld, Microfluidic bubble logic, *Science* **315**, 832 (2007).
- [85] L. R. Huang, E. C. Cox, R. H. Austin, and J. C. Sturm, Continuous particle separation through deterministic lateral displacement, *Science* **304**, 987 (2004).
- [86] D. F. Katz, J. R. Blake, and S. L. Paveri-Fontana, On the movement of slender bodies near plane boundaries at low Reynolds number, *J. Fluid Mech.* **72**, 529 (1975).
- [87] R. G. Winkler and G. Gompper, The physics of active polymers and filaments, *J. Chem. Phys.* **153**, 040901 (2020).